ADVANCED FUNCTIONAL MATERIALS
www.afm-journal.de

Highly-Packed Proximity-Coupled DC-Josephson Junction Arrays by a Direct-Write Approach

Fabrizio Porrati, Felix Jungwirth, Sven Barth, Gian Carlo Gazzadi, Stefano Frabboni, Oleksandr V. Dobrovolskiy, and Michael Huth*

Focused ion beam induced deposition (FIBID) is a direct-write technique enabling the growth of individual nanostructures of any shape and dimension with high lateral resolution. Moreover, the fast and reliable writing of periodically arranged nanostructures can be used to fabricate devices for the investigation of collective phenomena and to design novel functional metamaterials. Here, FIBID is employed to prepare dc-Josephson junction arrays (dc-JJA) consisting of superconducting NbC dots coupled through the proximity effect via a granular metal layer. The fabrication is straightforward and allows the preparation of dc-JJA within a few seconds. Microstructure and composition of the arrays are investigated by transmission electron microscopy and energy dispersive X-ray spectroscopy. The superconductor-to-metal transition of the prepared dc-JJA is studied in a direct way, by tuning the Josephson junction resistance in 70 nm-spaced superconducting NbC dots. The observed magnetoresistance oscillations with a period determined by the flux quantum give evidence for the coherent charge transport by paired electrons. Moreover, the measured resistance minima correspond to two fundamental matching configurations of fluxons in the dc-JJA, caused by magnetic frustration. The robust properties of the prepared dc-JJA demonstrate the opportunities for a fast preparation of complex device configurations using direct-write approaches.

1. Introduction

Currently, there is a great interest in the exploration of collective phenomena in nanosystems prepared by the direct-writing techniques of focused electron and ion beam induced deposition (FEBID and FIBID).[1–7] Their versatility regarding the substrate material, 3D writing capability, and sub-20 nm lateral resolution make these one-step additive techniques ideal candidates for the fabrication of JJA.[8–10] This interest is further increased by the fact that the fabrication of Josephson devices has so far been a complex, time-consuming multi-step process. Very recently, direct-write printing of single Josephson proximity junctions was demonstrated by FEBID of tungsten carbide.[11] At the same time, the development of 3D superconducting sensor arrays and quantum networks requires the understanding of the physics of superconductor-to-metal transition (SMT) and charge transport regimes in closely-packed JJA with tunable coupling strength.

The implementation of JJA started about 40 years ago, when they were considered as candidates for a new superconducting computer technology.[12] From that time on, JJA have been employed in research to model homogeneous ultrathin films and granular superconductors and to study phenomena like phase transitions, magnetic frustration, and vortex dynamics.[13] In the last years, several investigations suggest the use of JJA in quantum information, for example, as superinductances,[14] topologically protected qubits[15] and platforms for studying Majorana fermions,[16] in quantum metrology, for example, as current and voltage standards,[17–19] and in quantum electrodynamics.[20,21] JJA consist of superconducting units placed on a periodic lattice coupled via regions with suppressed superconductivity. A key aspect for the successful implementation of JJA is the ability to control precisely the energetics of the junctions, which governs the access to different electrical transport regimes.[13,22] In superconductor-normal metal-superconductor (SNS) arrays the coupling between neighboring superconducting islands determines whether the device works in the classical superconducting regime or in the quantum regime. Although JJA are usually prepared in the superconducting

F. Porrati, F. Jungwirth, S. Barth, M. Huth
Physikalisches Institut
Goethe-Universität
Max-von-Laue-Str. 1, D-60438 Frankfurt am Main, Germany
E-mail: porrati@physik.uni-frankfurt.de
G. C. Gazzadi, S. Frabboni
Istituto Nanoscienze
Consiglio Nazionale delle Ricerche
Via Campi, 213/A, 41125 Modena, Italy
S. Frabboni
FIM Department
University of Modena and Reggio Emilia
Via G. Campi 213/a, I-41125 Modena, Italy
O. V. Dobrovolskiy
Faculty of Physics
University of Vienna
Boltzmanngasse 5, A-1090 Vienna, Austria
The ORCID identification number(s) for the author(s) of this article can be found under https://doi.org/10.1002/adfm.202203889.

DOI: 10.1002/adfm.202203889

state,[23–25] various theoretical studies predict a quantum phase transition by tuning the Josephson coupling strength.[26] In particular, an SMT is expected for samples with large island spacings or with a low conductive 2D metal layer.[27–30] Indications of this transition were found in arrays of Nb islands coupled via a thin Au layer, as the number of islands per unit area was reduced below a critical value.[25,26] On the other hand, an experimental realization of JJA with tunable 2D metal layer to study the SMT is considered to be very challenging.[31] Therefore, up to now the SMT has been studied only indirectly on a Sn-graphene array system by gate-tuning the number of electrons in the graphene layer, which serve to vary the effective Josephson coupling between the Sn discs.[31]

In the present work, FIBID is employed to fabricate dc-JJA consisting of superconducting NbC dots coupled through the proximity effect via a thin granular metal layer with controllable dc electrical properties, which forms in situ during dot printing. Transmission electron microscopy (TEM) and energy dispersive X-ray spectroscopy (EDS) measurements reveal the microstructure and the composition of the dots and of the granular metal layer. The SMT of the system is studied in a direct way, that is, upon varying the thickness of the dots and the dc conductance of the granular metal layer. Magneto-resistance measurements indicate the emergence of metallic states and magnetic frustration visible by resistance oscillations. Thus, the investigation presented here illustrates the potential of the direct-write approach to tailor dc-Josephson devices ready to work in a specific transport regime, for applications and research purposes.

2. Results and Discussion

2.1. Fabrication

The samples were prepared by focused (Ga+) ion-beam induced deposition (FIBID) using the precursor $Nb(NMe_2)_3(N\text{-}t\text{-}Bu)$.[6,32] The dot structures were obtained by rastering the ion beam with 30 kV acceleration voltage, 10 pA beam current, 70 nm pitch, and 10 µs dwell time, respectively. The microstructure was investigated on arrays of dots written on areas of $4 \times 0.85\,\mu m^2$. In order to protect the dots and enhance the contrast during TEM/EDS measurements, a cover layer of Co_3Fe was deposited by FEBID.[4] Transport measurements were carried out on arrays written on areas of $3.5 \times \sim 0.49\,\mu m^2$, see **Figure 1**. After growth, an insulating layer was grown by FEBID using the same precursor[6] to locally protect the samples from oxidation, as detailed in the "Experimental Section." The deposition of each array took place within a few seconds.

2.2. Microstructure

The microstructure and chemical composition of the FIBID deposits were investigated by scanning/transmission electron microscopy (S/TEM). The investigation was carried out on three selected samples, labeled with *t*1, *t*2, and *t*3 of thickness 30, 50, and 90 nm. In **Figure 2**a is shown the high annular dark field (HAADF) TEM image of a lamella prepared from the dc-JJA array depicted as *t*2. The dots are slightly oblique, which can

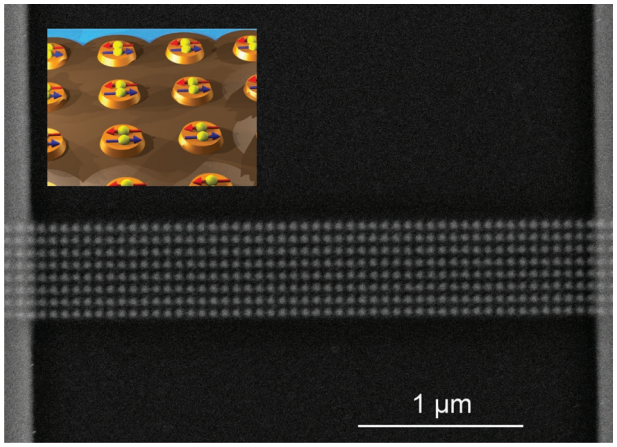

Figure 1. SEM image of a dc-Josephson junction array grown by FIBID using the $Nb(NMe_2)_3(N\text{-}t\text{-}Bu)$ precursor. The array is 3.5 µm long and 490 nm wide. The center-to-center distance between neighboring dots is 70 nm. The array is connected to gold electrodes for magnetotransport measurements.

be attributed either to charging effects or to ion beam astigmatism. Simultaneously to the FIBID deposition, etching effects caused by impinging Ga ions lead to a partial embedding of the dots in the SiO_2 substrate. The investigation of the microstructure shows that every dot is polycrystalline containing NbC nanocrystals with sizes up to 10–20 nm according to the bright field TEM image (Figure S1a,b, Supporting Information). The cubic NbC crystal phase is found by micro-diffraction carried out on single nanocrystals using Si as reference (Figure S1c,d, Supporting Information), in analogy to recently investigated NbC 3D nanowires and planar nanostructures.[6]

EDS was carried out in STEM acquisition mode to image the spatial elemental distribution. EDS maps of the corresponding HAADF image associated to sample *t*2 is illustrated in Figure 2 showing the localization of Nb, Ga, and the Fe signal of the FEBID-Co_3Fe protection layer. Nb, see Figure 2b, is localized in the entire dots and in the region between them, forming a Nb-based thin layer close to the surface, as a consequence of the simultaneous electron-beam deposition as a secondary effect during ion irradiation. Note that during the raster movement the ion beam is not blanked, which causes additional deposition of material in the inter-dot region. Moreover, the local distribution of Ga, depicted in Figure 2d, illustrates the incorporation in the dots as well as its extension into the SiO_2 substrate material due to implantation effects. EDS line-scans of the inter-dot region and on a dot toward the substrate material are plotted in Figure 2c. According to this analysis, the dots contain Nb and C, as well as Ga, with the highest Ga concentration located underneath the NbC dots, which is also represented as bright spots in the dark region of the HAADF image associated with the SiO_2 substrate material in Figure 2a due to *Z*-contrast. Note that the fractional value of C might be affected by hydrocarbon contamination, which was however minimized by plasma cleaning the lamellae prior investigation. The line scan in the inter-dot region shows similar elemental distribution as expected for a thin Nb-based layer and an additional Ga implantation depth of 30–40 nm in the initial SiO_2 substrate. Since both, the implanted Ga as well as the Nb-based

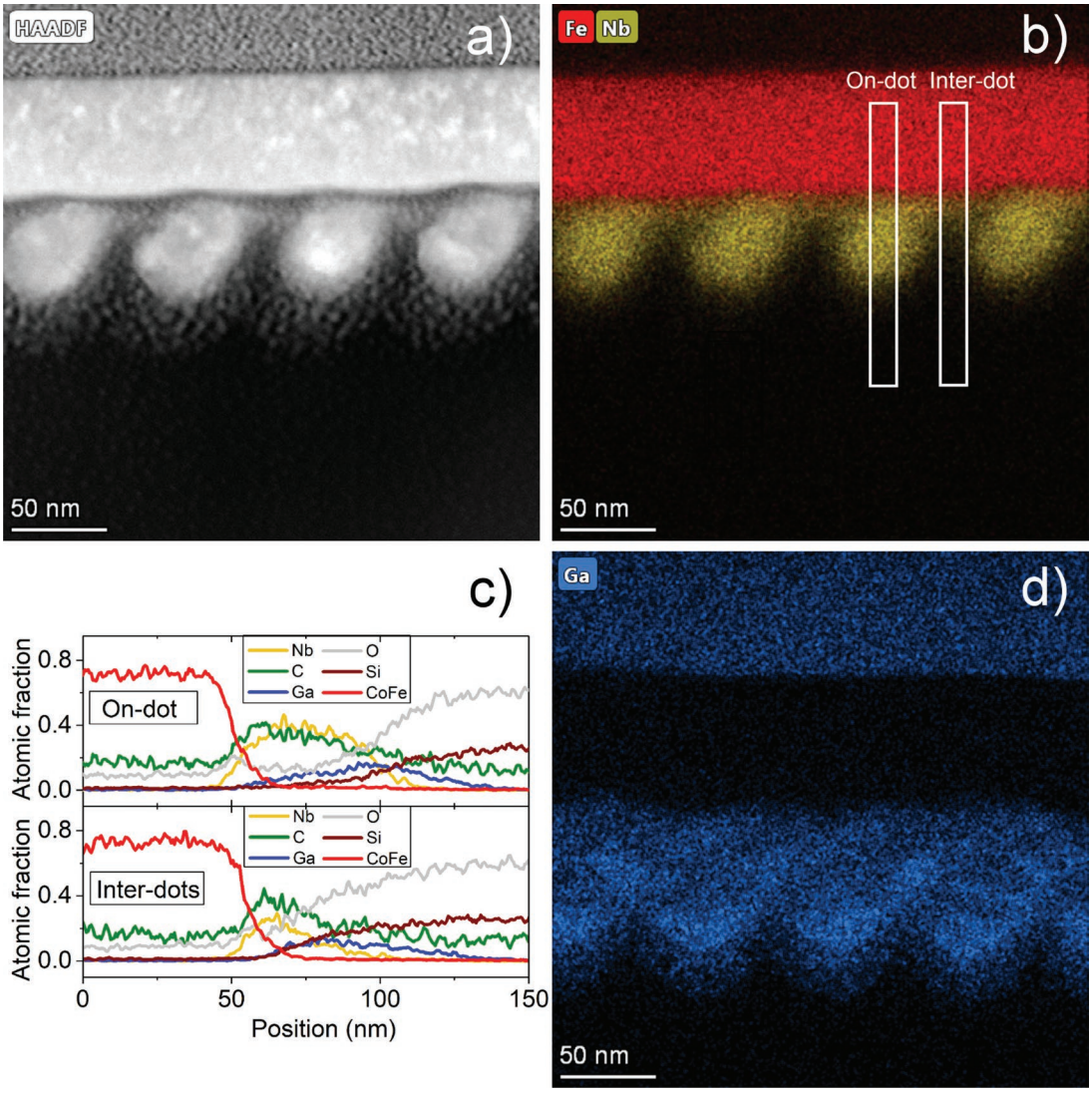

Figure 2. a) STEM-HAADF image of a dot-array with inter-dot distance equal to 70 nm. The array is protected with a Co_3Fe/PtC double-layer. b,d) 2D STEM-EDS compositional analysis of the dot region. The images show the spatial distribution of Nb, Fe, and Ga, respectively. c) Line-scans of the inter-dot and on-dot regions.

layer is located between the NbC dots, the electrical coupling of neighboring NbC dots could be facilitated either by the Nb-based layer, the Ga implantation layer or a combination thereof. A similar analysis has been carried out for samples *t*1 and *t*3, see Figures S2 and S3, Supporting Information. A comparison of the three HAADF micrographs reveals a widening of the dots with the number of passes used for their fabrication. As a consequence, the edge-to-edge inter-dot spacing is reduced with the dot thickness, promoting coupling of neighboring dots. EDS reveals a similar composition of the Nb-based inter-dot layer for all three samples examined but different thicknesses, as visible by comparing the line-scans in the inter-dot regions, with the evolvement of a crystalline NbC layer as illustrated for sample *t*3 for samples with higher number of passes in the fabrication step, see Figure S3a, Supporting Information. In addition, the material between individual dots always contains a 30–40 nm thick Ga-SiO_2 layer formed by implantation.

2.3. Magnetotransport Properties

Transport measurements were carried out on a series of five samples, labeled with s3, s4, s7, s10, and s12, respectively, which reflects the number of beam passes used during the growth, namely, 3000, 4000,.. etc. According to the calibration carried out by atomic force microscopy (AFM), see Figure S8, Supporting Information, the thicknesses of these samples are between 15 and 45 nm. **Figure 3** presents the temperature dependence of the normalized resistance $R(T)/R_{285\,K}$ in the range 20–285 K. The $R(T)$ curves of all samples exhibit a monotonic behavior with negative temperature coefficient $\alpha = dR/dT < 0$, which is typical for granular metals in the quasi-metallic regime.[33] At low temperatures, proximity-coupled JJA are expected to be superconducting.[23] In order to illustrate the behavior of the NbC dot arrays, in **Figure 4**a we plot exemplary the enlarged low-temperature part of the $R(T)$ curve of sample s7.

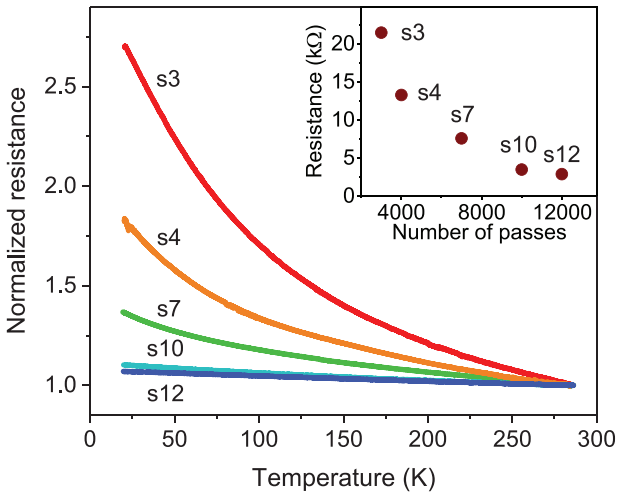

Figure 3. Temperature dependence of the normalized resistance $R(T)/R(285)$ in the range 20–285 K for the set of samples investigated in the present work. The thickness of the samples varies from 15 nm (s3, red curve) to 45 nm (s12, dark blue curve). Inset: Room-temperature resistance versus number of passes used to fabricate the sample, see also Supporting Information for the calibration of the thickness versus the number of passes.

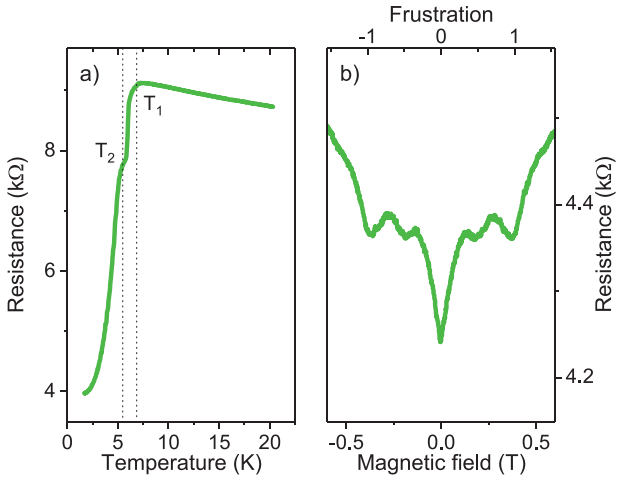

Figure 4. a) Low temperature dependence of the resistance of sample s7. The sample exhibits a first transition at $T_1 = 6.9 \approx$ K, where local phase coherence sets in the NbC dots. A second transition starts at $T_2 = 5.4$ K, where global phase coherence develops in the entire dc-Josephson junction array, see also Figure 5. The non-zero resistance in the limit of zero temperature is due to an intervening metallic state. b) Magnetic field dependence of the resistance of sample s7 at 1.4 K. The resistance exhibits two dips at $B = 0.38$ T and $B = 0.19$ T, close to the theoretical predicted values for the frustration parameter $f = 1$ and $f = 1/2$, respectively. The corresponding vortex configuration are sketched in Figure 6c,d.

In the range 20–7 K, the resistance increases following the behavior observed at higher temperatures. At the temperature $T_1 = 6.9$ K a first resistance drop occurs, where local phase coherence sets in within the NbC dots,[23] as illustrated in **Figure 5**. At lower temperatures, superconducting correlations are induced in the co-deposit layer due to the proximity effect as both, the coherence length ξ_N of the normal-metal layer and the interdot Josephson coupling increase. At T_2, when ξ_N is comparable with the interdot spacing, global phase coherence in the entire system emerges.[25,34] The establishment of global phase coherence at 1.4 K, the lowest temperature reached in the experiment, is robust since $2\xi_N(1.4\,\text{K}) \approx 30$ nm is equal to the edge-to-edge distance between the islands in the JJA. This can be estimated by considering the electron diffusivity coefficient $D \approx 0.5$ cm^2 s^{-1} for superconducting NbC deposits[7] so that $\xi_N = (\hbar D/(k_B T))^{1/2} \approx 15$ nm for the proximity length in a normal-metal layer.

Below T_2, the perpendicular magnetoresistance $R(B)$ of samples s7 and s10 oscillates at low fields, see Figures 4b and 7b. The $R(B)$ curves of samples s7 and s10 are symmetric under field polarity reversal, and the $R(B)$ oscillations appear on a monotonically rising background. The appearance of $R(B)$ oscillations in periodic superconducting systems relates to the commensurability of the vortex configuration with the

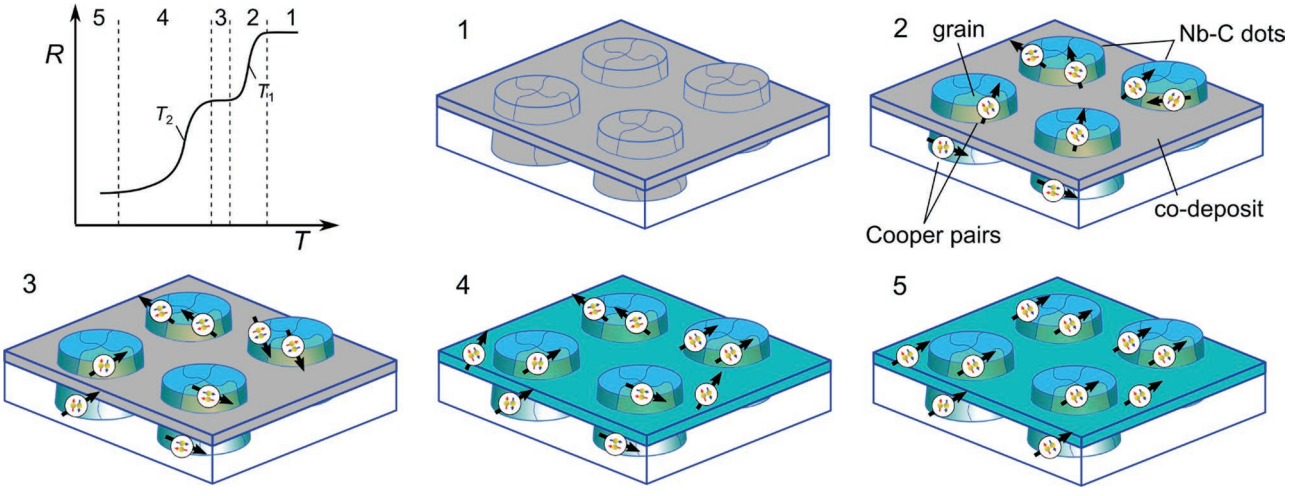

Figure 5. Different electric charge transport regimes upon cooling the dc-Josephson junction array. Above T_c the entire system is in the normal state (1). At T_1, superconductivity sets in within individual grains (2) and reaches phase coherence within the dots (3). Arrows designate the phase of the wave function. At T_2 superconducting correlations are induced in the co-deposit layer (4), leading to phase coherence in the entire dc-JJA (5).

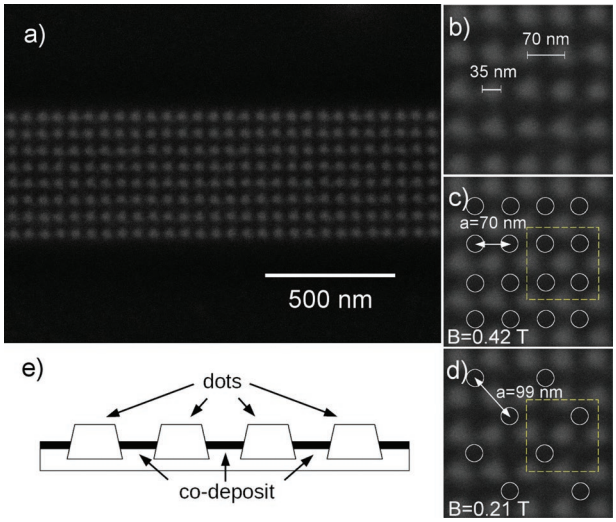

Figure 6. a) SEM image of a NbC dc-Josephson junction array grown by FIBID. b) Details of the array structure. The dot diameter is about 35 nm; the center-to-center distance between neighboring dots is 70 nm. The superconducting NbC dots are coupled to each other via a thin granular metal layer (co-deposit) through the proximity effect (e). Configurations of vortices (designated by white circles) at 0.42 T (c) and 0.21 T (d), respectively, see text for details. Dashed lines encage regions containing four elementary cells.

underlying sample periodicity.[24,35–37] In the following, the oscillations of the NbC arrays are discussed in the framework of the model for JJA. This choice is justified by preliminary measurements of the Shapiro response in *I*–*V*-characteristics subjected to a radio frequency (RF) excitation. A detailed account on the high-frequency behavior of the JJA is planned in a forthcoming publication. In the classical regime, proximity-coupled arrays exhibit magnetic frustration, when a magnetic field is applied perpendicularly to the device.[24,36,38] In the applied magnetic field vortices form and, above the depinning current, they move causing a resistance, which grows linearly with the field,[13] see Figure 4b. The Hamiltonian of the JJA neglecting charging effects is given by $H = -E_J\sum_{ij}\cos(\phi_i - \phi_j - A_{ij})$,[39,40] with E_j being the coupling energy, which is proportional to the order parameter amplitude on the islands, $\phi_{i,j}$ the phase in the dots i and j, and $A_{i,j} = (2\pi/\phi_0)\int_i^j \mathbf{A}\cdot\mathbf{dl}$ with $\mathbf{A}$ the magnetic vector potential. The Hamiltonian has a period $f = 1$, where a minimum in the resistance is expected. The frustration parameter $f = \sum_{cell}A_{ij}/2\pi = BS/\phi_0$ is the magnetic flux BS threading the unit cell of the array, with area S, divided by the flux quantum ϕ_0. In a square array with lattice constant $a = 70$ nm, the minimum is expected at $B = 0.42$ T, see **Figure 6**c, which is close to the $B = 0.38$ T observed in our experiment, see Figure 4b. In JJA several ground state vortex configurations are possible, which are stable against the bias current, thus leading to dips in the electrical resistance,[13,39] as the one measured for $f = \pm 1/2$, corresponding to 0.19 T, see also Figure 6d. The appearance of the charge $2e$ in the period of quantum oscillations, which is $\phi_0 = h/2e$, indicates an electrical transport due to paired electrons, as shown recently in nanopatterned YBCO thin films around the SIT.[38] The magnetoresistance oscillations originate from Cooper pair quantum interference effects in the multiply connected geometry imposed by the JJA structure. These effects enter through the Josephson coupling energy between nodes of the JJA, requiring the line integral of the phase around a closed loop be a multiple of 2π. In the investigated regime, the magnetoresistance oscillates because E_j acts as a barrier to thermally-activated and current-driven vortex motion.

Figure 7 illustrates the superconductor-to-metal transition of the system. We divide the samples in two groups: those with normal state resistance $R_N < R_Q$, being R_Q the quantum

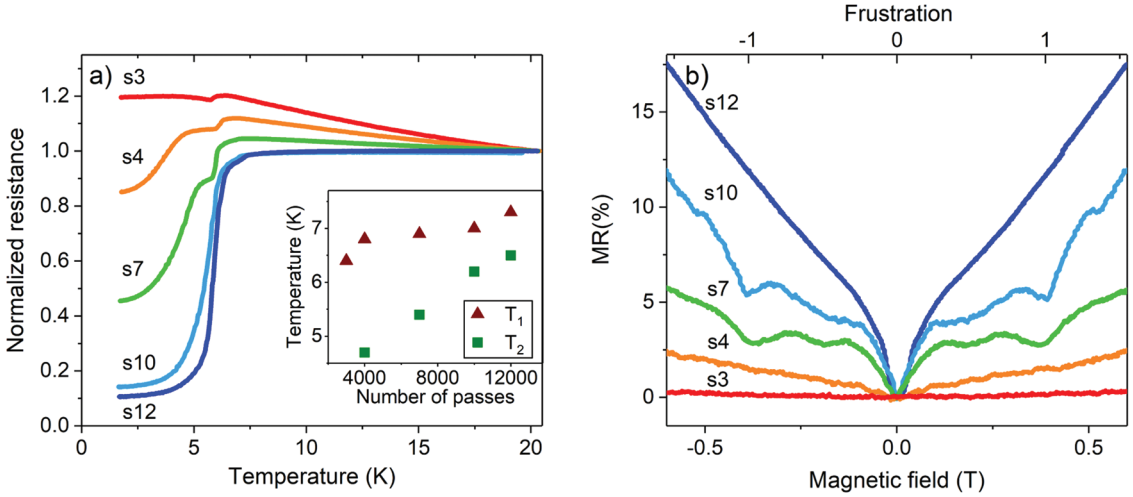

Figure 7. a) Low temperature dependence of the normalized resistance $R(T)/R(20)$ in the range 1.7–20 K for the set of samples investigated. Un-paired electrons dominate the transport in thinner samples, such as s3, characterized by a normal resistance $R_N > R_Q$, being R_Q the quantum resistance. Paired electrons dominate the transport in thicker samples, such as s12, with $R_N < R_Q$. See also Figure S5, Supporting Information. Inset: Dependence of the transition temperatures T_1 and T_2 on the number of passes used to fabricate the sample. b) Magnetoresistance measured at 1.4 K for the set of samples investigated. Samples s7 and s10 exhibit frustration with oscillations at 0.38 and 0.19 T. The other samples do not show frustration for different reasons, such as the absence of paired electrons (s3), the non-coherent transport of paired electrons (s4), and the thickness of the co-deposit, which does not behave as weak link (s12). Note that in the figure the curve of sample s12 is scaled by a factor 2/3.

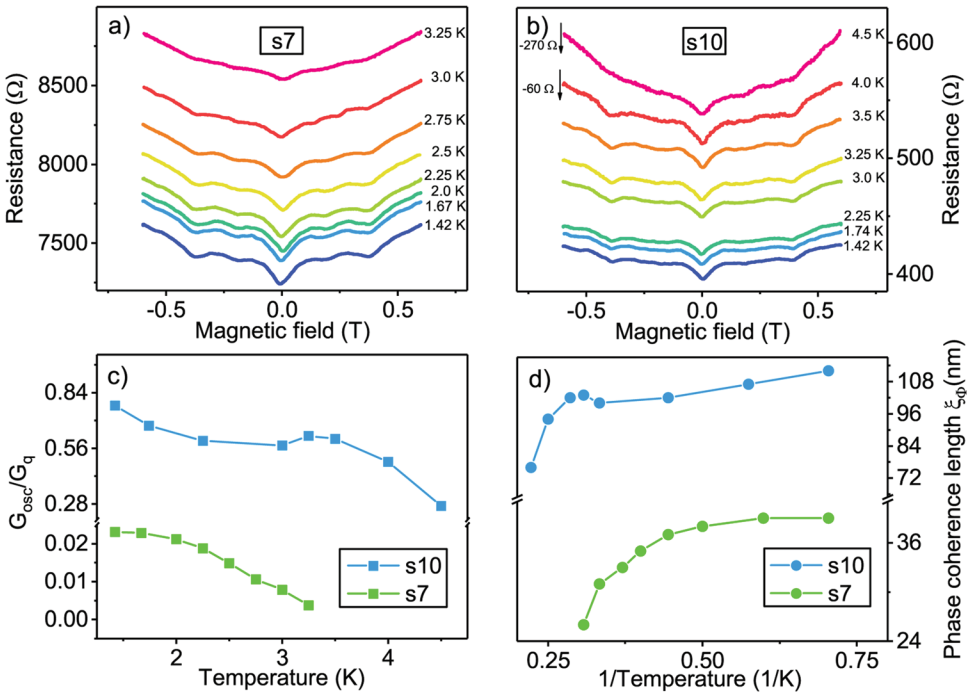

Figure 8. Dependence of the resistance on the perpendicular magnetic field for different temperatures for samples s7 (panel a) and s10 (panel b). A bias current of 20 μA was used for the measurements. c) Temperature dependence of the conductance oscillations G_{osc}, normalized to the conductance quantum G_q. The oscillations are extracted from the conductance after subtraction of the background; see also Figure S10, Supporting Information. d) Phase coherence length ξ_ϕ versus temperature for samples s7 and s10. In general, at low temperatures ξ_ϕ is expected to be constant in metallic systems and to diverge in superconductors.

resistance $h/(2e)^2$ = 6.4 kΩ, that is, s10 and s12, which are expected to become superconducting at low temperatures, and those with $R_N > R_Q$, that is, s3, s4, and s7, see Figure S5, Supporting Information. In Figure 7a we depict the low temperature behavior of the resistance in the range 1.8–20 K. The transition temperatures T_1 and T_2 decrease monotonically with the dot thickness. For T_1 this behavior can be attributed to an increased number of defects in thinner dots with lower degree of structural order as well as crystal and grain size, which is known to reduce T_c, for instance in Nb thin films.[41–43] For T_2 the decrease is due to the reduction of the coupling strength as a consequence of the decrease of the diameter of the dots, as shown by comparing the three HAADF micrographs in Figure 2 and Figures S2 and S3, Supporting Information. The resistance of samples s10 and s12 is constant in the range 20–7 K. At lower temperature the resistance flattens out to a constant value. For these sample thicknesses, the existence of a residual resistance is a consequence of the two-probe configuration chosen for the measurement. By using a four-probe configuration the residual resistance disappears. A comparison between two-probe and four-probe measurements is reported in Figure S6, Supporting Information. For thinner samples we observe an increase of the residual resistance, which is explained by the corresponding reduction of the co-deposit thickness, as visible from the inter-dot scans in Figure 2 and Figures S2 and S3, Supporting Information. Furthermore, compositional inhomogeneities either around the dots, due to the raster pattern, or in the co-deposit thickness, as found in other systems prepared by FIBID,[44] might play a role.

In Figure 7b we plot the magnetic field dependence of the resistance of the samples in the range −0.6 T ≤ B ≤ 0.6 T. Sample s12 exhibits a linear increase of the resistance at low fields, but no frustration effects. The absence of oscillations indicates that the co-deposit does not function as a weak link in the SNS junction. This is likely due to the diameter of the NbC-dots which have coalesced, as in sample *t*3, forming a continuous superconducting layer. For sample s10 frustration starts to emerge since separated NbC-dots are coupled through the granular metal layer. Samples s4 and s7 show a drop of the resistance below 6 K indicating the formation of Cooper pairs. However, oscillations are present only in s7. Therefore, we deduce that paired electrons move coherently in s7 and non-coherently in s4, though here the absence of oscillations might be due to our instrumental resolution limits. Finally, s3 does not show any resistance drop at low temperature, indicating a transport exclusively due to unpaired electrons. To gather more information about the character of the states, we investigate the temperature dependence of the oscillations for samples s7 and s10, see **Figure 8**a,b. In particular, the oscillation amplitude of the conductance G_{osc} has been analyzed. This allows the calculation of the phase coherence length ξ_ϕ by the expression $G_{osc} = \frac{4e^2}{h}\left(\frac{\xi_\phi}{\pi r}\right)^{1.5} \exp\left(-\frac{\pi r}{\xi_\phi}\right)$,[38,45] where r is half the center-to-center distance between neighboring dots, that is, r = 35 nm. Figure 8c,d shows the normalized conductance oscillation amplitude G_{osc}/G_q, with $G_q = 2e^2/h$ the conductance quantum, and the phase coherence length ξ_ϕ, respectively. G_{osc} is presented after subtraction of the rising background, see

Figure S10, Supporting Information. In general, ξ_ϕ is expected to quench abruptly across the SIT in fermionic systems, while it gradually decreases in bosonic ones.[46] In the latter case, at low temperatures ξ_ϕ diverges for superconductors, it is constant for metals and it tends to zero for insulators.[38] The analysis of sample s7 shows at the lowest temperature a value of ξ_ϕ equal to 39 nm which is very close to the edge-to-edge distance between two neighboring dots, see SEM image in Figure 6. Therefore paired electrons are delocalized and free to move in the sample. This is confirmed by the saturation of ξ_ϕ at low temperatures, which characterizes the system as a metal. The behavior of sample s10 is analogous. However, both the larger value of ξ_ϕ and its slightly increasing value at low temperatures indicate in this case a metallic sample close to becoming superconducting.

3. Conclusions

In this work, the direct fabrication of highly-packed proximity-coupled dc-Josephson junction arrays by focused-ion-beam induced deposition has been demonstrated. The analysis of the microstructure reveals that the dc-JJA consist of NbC dots coupled via a thin granular metal layer composed of C, Nb, and Ga. The tunability of the coupling, which is controlled by the conductance of the granular metal layer, allows for the study of the superconductor-to-metal transition, moving from the classical superconducting regime into the quantum regime. In particular, low-temperature transport measurements suggest that in the classical regime, charge transport is dominated by paired electrons with evidence of magnetoresistance oscillations due to magnetic frustration. By moving from the classical to the quantum regime, charge transport by paired electrons first becomes incoherent and then disappears for very thin samples, where unpaired electrons dominate the transport. In conclusion, the fabrication of highly packed proximity-coupled NbC dc-Josephson-junction arrays with tunable coupling strength is an essential step toward the development of Josephson devices ready to work in a specific transport regime, for applications, for example, in metrology and quantum computing and research purposes, enabling investigations of phase transitions, magnetic frustration, and vortex dynamics.

4. Experimental Section

Fabrication: The samples were fabricated by FIBID in a dual beam FIB/SEM microscope (FEI, Nova NanoLab 600) equipped with a Schottky electron emitter. In FIBID (FEBID) the adsorbed molecules of a precursor gas injected inside a microscope dissociate by interaction with the ion (electron) beam, forming the sample during the rastering process. Furthermore, during the FIBID fabrication process scattered Ga^+ ions (electrons) dissociate precursor molecules around the dots, forming a granular layer around the written structure.[47,48] The precursor employed, $Nb(NMe_2)_3$(N-t-Bu), was synthesized as described in literature.[6,32] The precursor was introduced in the reaction chamber using a standard FEI gas-injection system equipped with a capillary of about 0.5 mm inner diameter. The precursor was maintained at a temperature of 35 °C to ensure sufficient volatility. The distance capillary-substrate was about 100 µm. The angle between capillary and ion (electron) beam was 35° (55°). The base pressure of the microscope was about 5×10^{-7} mbar. The pressure during deposition was about 2×10^{-6} mbar. The samples were fabricated by FIBID with the parameters reported in the main text. For transport measurements, a protecting layer was deposited by FEBID using the same precursor with the following electron beam parameters: 5 keV acceleration voltage, 0.4 nA beam current, 20 nm pitch, 1 µs dwell time, and 5 nC μm^{-2} electron dose, respectively.[6] For TEM/EDS measurements, a cover layer of Co_3Fe was deposited by FEBID using the $HFeCo_3(CO)_{12}$ precursor and as electron beam parameters 5 keV acceleration voltage, 1.6 nA beam current, 20 nm pitch, and 1 µs dwell, respectively.[4] The samples were prepared on Si(p-doped)/SiO_2 (200 nm) substrates and connected to NbC bridge-electrodes, prepared by FIBID with 30 keV acceleration voltage, 10 pA beam current, 30 nm pitch, and 200 ns dwell time, respectively. The NbC bridge-electrodes were attached to 50 nm thick Au/Cr electrodes prepared by standard lithography for two-probe electrical transport measurements.

Sample Characterization: Lamellae for the investigation of the microstructure were prepared by focused ion beam lift-out with a dual beam FEI Strata 235 M. Before milling, the samples were protected by PtC overlayer grown by FIBID. The S/TEM and EDS investigations were carried out on a Talos F200S G2 S/TEM equipped with a Schottky field emitter and fast EDS mapping. Electrical transport measurements were carried out in the range 1.4–285 K using a variable-temperature insert in a ^{4}He cryostat equipped with a 12 T superconducting solenoid employing a Keithley Sourcemeter 2635B and an Agilent 34420A nanovoltmeter. The thickness of the samples was measured by AFM in non-contact mode (nanosurf, easyscan2).

Supporting Information

Supporting Information is available from the Wiley Online Library or from the author.

Acknowledgements

S.B. acknowledges funding by the Deutsche Forschungsgemeinschaft (DFG) through Grant Nos. BA 6595/2-1 and BA 6595/1-1. Support through the Frankfurt Center of Electron Microscopy (FCEM) and the European Cooperation in Science and Technology via COST Action No. CA16218 (NANOCOHYBRI) are gratefully acknowledged.

Open access funding enabled and organized by Projekt DEAL.

Conflict of Interest

The authors declare no conflict of interest.

Data Availability Statement

The data that support the findings of this study are available from the corresponding author upon reasonable request.

Keywords

direct-write fabrications, focused ion beam induced depositions, Josephson junction arrays, magnetic frustration, nanolithography, NbC, superconductor-to-metal transition

Received: April 6, 2022
Revised: June 14, 2022
Published online: July 1, 2022

[1] M. Esposito, V. Tasco, M. Cuscun, F. Todisco, A. Benedetti, I. Tarantini, M. D. Giorgi, D. Sanvitto, A. Passaseo, *ACS Photonics* **2015**, *2*, 105.

[2] R. Córdoba, D. Mailly, R. O. Rezaev, E. I. Smirnova, O. G. Schmidt, V. M. Fomin, U. Zeitler, I. Guillamón, H. Suderow, J. M. De Teresa, *Nano Lett.* **2019**, *19*, 8597.
[3] R. Sachser, F. Porrati, M. Huth, *Phys. Rev. B* **2009**, *80*, 195416.
[4] F. Porrati, M. Pohlit, J. Müller, S. Barth, F. Biegger, C. Gspan, H. Plank, M. Huth, *Nanotechnology* **2015**, *26*, 475701.
[5] O. V. Dobrovolskiy, R. Sachser, S. A. Bunyaev, D. Navas, V. M. Bevz, M. Zelent, W. Smigaj, J. Rychly, M. Krawczyk, R. V. Vovk, M. Huth, G. N. Kakazei, *ACS Appl. Mater. Interf.* **2019**, *11*, 17654.
[6] F. Porrati, S. Barth, R. Sachser, O. V. Dobrovolskiy, A. Seybert, A. S. Frangakis, M. Huth, *ACS Nano* **2019**, *13*, 6287.
[7] O. V. Dobrovolskiy, D. Y. Vodolazov, F. Porrati, R. Sachser, V. M. Bevz, M. Y. Mikhailov, A. V. Chumak, M. Huth, *Nat. Commun.* **2020**, *11*, 3291.
[8] M. Huth, F. Porrati, O. V. Dobrovolskiy, *Microelectr. Engin.* **2018**, *185-186*, 9.
[9] A. Fernandez-Pacheco, L. Skoric, J. De Teresa, J. Pablo-Navarro, M. Huth, O. V. Dobrovolskiy, *Materials* **2020**, *13*, 3774.
[10] M. Huth, F. Porrati, S. Barth, *J. Appl. Phys.* **2021**, *130*, 170901.
[11] T. J. Blom, T. W. Mechielsen, R. Fermin, M. B. S. Hesselberth, J. Aarts, K. Lahabi, *ACS Nano* **2021**, *15*, 322.
[12] R. F. Voss, R. A. Webb, *Phys. Rev. B* **1982**, *25*, 3446.
[13] R. Fazio, H. van der Zant, *Phys. Rep.* **2001**, *355*, 235.
[14] N. A. Masluk, I. M. Pop, A. Kamal, Z. K. Minev, M. H. Devoret, *Phys. Rev. Lett.* **2012**, *109*, 137002.
[15] S. Gladchenko, D. Olaya, E. Dupont-Ferrier, B. Douçot, L. B. Ioffe, M. E. Gershenson, *Nat. Phys.* **2009**, *5*, 48.
[16] B. van Heck, A. R. Akhmerov, F. Hassler, M. Burrello, C. W. J. Beenakker, *N. J. Phys.* **2012**, *14*, 035019.
[17] I. M. Pop, I. Protopopov, F. Lecocq, Z. Peng, B. Pannetier, O. Buisson, W. Guichard, *Nat. Phys.* **2010**, *6*, 589.
[18] K. Cedergren, R. Ackroyd, S. Kafanov, N. Vogt, A. Shnirman, T. Duty, *Phys. Rev. Lett.* **2017**, *119*, 167701.
[19] R. Behr, O. Kieler, J. Kohlmann, F. Müller, L. Palafox, *Meas. Sci. Technol.* **2012**, *23*, 124002.
[20] R. Kuzmin, R. Mencia, N. Grabon, N. Mehta, Y.-H. Lin, V. E. Manucharyan, *Nat. Phys.* **2019**, *15*, 930.
[21] J. Puertas Martínez, S. Léger, N. Gheeraert, R. Dassonneville, L. Planat, F. Foroughi, Y. Krupko, O. Buisson, C. Naud, W. Hasch-Guichard, S. Florens, I. Snyman, N. Roch, *npj Quantum Inform.* **2019**, *5*, 19.
[22] R. S. Newrock, C. J. Lobb, U. Geigenmüller, M. Octavio, *The Two-Dimensional Physics of Josephson Junction Arrays*, Vol. *54*, Academic Press, Cambridge, MA **2000**, pp. 263–512.
[23] D. J. Resnick, J. C. Garland, J. T. Boyd, S. Shoemaker, R. S. Newrock, *Phys. Rev. Lett.* **1981**, *47*, 1542.
[24] D. Kimhi, F. Leyvraz, D. Ariosa, *Phys. Rev. B* **1984**, *29*, 1487.
[25] S. Eley, S. Gopalakrishnan, P. M. Goldbart, N. Mason, *Nat. Phys.* **2012**, *8*, 59.
[26] A. Kapitulnik, S. A. Kivelson, B. Spivak, *Rev. Mod. Phys.* **2019**, *91*, 011002.
[27] M. V. Feigel'man, A. I. Larkin, *Chem. Phys.* **1998**, *235*, 107.
[28] M. V. Feigel'man, A. I. Larkin, M. A. Skvortsov, *Phys. Rev. Lett.* **2001**, *86*, 1869.
[29] B. Spivak, A. Zyuzin, M. Hruska, *Phys. Rev. B* **2001**, *64*, 132502.
[30] B. Spivak, P. Oreto, S. A. Kivelson, *Phys. Rev. B* **2008**, *77*, 214523.
[31] Z. Han, A. Allain, H. Arjmandi-Tash, K. Tikhonov, M. Feigel'man, B. Sacépé, V. Bouchiat, *Nat. Phys.* **2014**, *10*, 380.
[32] A. Baunemann, D. Bekermann, T. B. Thiede, H. Parala, M. Winter, C. Gemel, R. A. Fischer, *Dalton Trans.* **2008**, *28*, 3715.
[33] M. Huth, F. Porrati, C. Schwalb, M. Winhold, R. Sachser, M. Dukic, J. Adams, G. Fantner, *Beilstein J. Nanotechnol.* **2012**, *3*, 597.
[34] S. Eley, *Ph.D. Thesis*, University of Illinois **2012**.
[35] H. S. J. van der Zant, W. J. Elion, L. J. Geerligs, J. E. Mooij, *Phys. Rev. B* **1996**, *54*, 10081.
[36] M. Durkin, I. Mondragon-Shem, S. Eley, T. L. Hughes, N. Mason, *Phys. Rev. B* **2016**, *94*, 024510.
[37] I. G. Serrano, J. Sesé, I. Guillamón, H. Suderow, S. Vieira, M. R. Ibarra, J. M. De Teresa, *Beilstein J. Nanotechnol.* **2016**, *7*, 3446.
[38] C. Yang, Y. Liu, Y. Wang, L. Feng, Q. He, J. Sun, Y. Tang, C. Wu, J. Xiong, W. Zhang, X. Lin, H. Yao, H. Liu, G. Fernandes, J. Xu, J. M. Valles, J. Wang, Y. Li, *Science* **2019**, *366*, 1505.
[39] S. Teitel, C. Jayaprakash, *Phys. Rev. Lett.* **1983**, *51*, 1999.
[40] P. Martinoli, C. Leemann, *J. Low Temp. Phys.* **2000**, *118*, 699.
[41] S. Bose, P. Raychaudhuri, R. Banerjee, P. Vasa, P. Ayyub, *Phys. Rev. Lett.* **2005**, *95*, 147003.
[42] C. Delacour, L. Ortega, M. Faucher, T. Crozes, T. Fournier, B. Pannetier, V. Bouchiat, *Phys. Rev. B* **2011**, *83*, 144504.
[43] O. V. Dobrovolskiy, M. Huth, *Thin Solid Films* **2012**, *520*, 5985.
[44] A. Fernández-Pacheco, J. M. De Teresa, R. Córdoba, M. R. Ibarra, *Phys. Rev. B* **2009**, *79*, 174204.
[45] F. Pierre, A. B. Gougam, A. Anthore, H. Pothier, D. Esteve, N. O. Birge, *Phys. Rev. B* **2003**, *68*, 085413.
[46] S. M. Hollen, G. E. Fernandes, J. M. Xu, J. M. Valles, *Phys. Rev. B* **2013**, *87*, 054512.
[47] I. Utke, P. Hoffmann, J. Melngailis, *J. Vac. Sci. Technol., B: Microelectron. Nanometer Struct.–Process., Meas., Phenom.* **2008**, *26*, 1197.
[48] R. Córdoba, *Functional Nanostructures Fabricated by Focused Electron/Ion Beam Induced Deposition*, Springer, Berlin **2014**.